Monkey brain cortex imaging by photoacoustic tomography

Xinmai Yang
Lihong V. Wang
Washington University in St. Louis
Department of Biomedical Engineering
Optical Imaging Laboratory
St. Louis, Missouri, 63130

Abstract. Photoacoustic tomography (PAT) is applied to image the brain cortex of a monkey through the intact scalp and skull *ex vivo*. The reconstructed PAT image shows the major blood vessels on the monkey brain cortex. For comparison, the brain cortex is imaged without the scalp, and then imaged again without the scalp and skull. Ultrasound attenuation through the skull is also measured at various incidence angles. This study demonstrates that PAT of the brain cortex is capable of surviving the ultrasound signal attenuation and distortion caused by a relatively thick skull. [DOI: 10.1117/1.2967907]

Keywords: photoacoustics; imaging; monkey brain; tomography; skull.

Paper 07471R received Nov. 25, 2007; revised manuscript received Mar. 3, 2008; accepted for publication Mar. 4, 2008; published online Aug. 20, 2008.

1 Introduction

High-resolution human brain imaging modalities currently used in clinics include X-ray computerized tomography (CT) and magnetic resonance imaging (MRI). However, both CT and MRI are expensive. Furthermore, X-ray CT involves exposure to ionizing radiation. In certain cases, ultrasound brain imaging is employed.[1] Ultrasound imaging is an established pediatric brain imaging modality[2] for use before the fontanelles are closed. After the closure of the fontanelles, the image quality degrades significantly because the skull severely attenuates and scatters ultrasonic waves. Transcranial ultrasonic brain imaging of adults is also limited by the inhomogeneous aberrating effect of the skull bone.[3–9] The skull bone induces both phase and amplitude distortions. Such distortions can be potentially corrected by various methods, such as adaptive focusing,[10] time reversal,[11] dynamic focusing,[12] and spatiotemporal inverse filter (STIF).[13] However, transcranial ultrasound imaging still suffers from poor resolution and poor contrast.

Photoacoustic tomography (PAT) is a hybrid, non-ionizing imaging modality, which combines the resolution of ultrasound imaging with the contrast of optical imaging.[14–18] In PAT, pulsed laser energy is delivered into biological tissue. The subsequent ultrasound signal generated by the photoacoustic (PA) effect is detected to form an image through a reconstruction algorithm. Compared with pure ultrasound imaging, the contrast in PAT is optically based. PAT is particularly suitable for imaging blood vessels because of the high optical contrast between blood and surrounding biological tissue. In addition, PAT detects ultrasound signals through one-way propagation. Therefore, PAT suffers less distortion by the skull than ultrasound imaging.

Brain cortex imaging by PAT, including structural, functional, and molecular imaging, has been successfully conducted in small animals.[19,20] However, brain cortex imaging with PAT in large animals has not been studied. Our group has reported monkey brain imaging using thermoacoustic tomography (TAT).[21] Compared with TAT, whose contrast is determined by the water content and ion concentration of biological tissues, PAT provides dominantly hemoglobin contrast and is more suitable for vascular imaging.

We extend the application of PAT to large animal brain cortex imaging in this study. One monkey head sample was imaged with our PAT system. Although the skull of the monkey head was as thick as ~2 mm, the main structures of the monkey brain cortex were identified by PAT. This promising result shows the feasibility of large animal brain cortex imaging using PAT.

2 Methods and Materials

The experimental setup for this study is shown in Fig. 1. A Q-switched Nd:YAG laser (pulse width: <15 ns) (LS-2137/2, Symphotic TII Co., Camarillo, CA), operating at 1064 nm with a pulse repetition rate of 10 Hz, was employed as the irradiation source. A monkey head sample was irradiated from the top, and PA signals were detected on the orthogonal plane by an ultrasound transducer and then amplified by a 50-dB amplifier (5072 PR, Panametrics, Waltham, MA). Next, the signals were directed to a digital oscilloscope (TDS5054, Tektronix, Beaverton, OR) and collected through a PC.

The early work by Fry[22] showed that ultrasound signals propagating through a skull suffer from less distortion at lower frequencies (0.5–1 MHz). Therefore, an unfocused ultrasonic transducer (V303, Panametrics, Waltham, MA) with a center frequency of 1 MHz and 60% bandwidth was used in our experiment. The active element size of the transducer is 12 mm.

A fresh head sample of a 20-month-old rhesus monkey was obtained from the California Primate Research Center. The head sample was immersed in a 10% formalin solution

Address all correspondence to: Lihong V. Wang, Optical Imaging Lab, Department of Biomedical Engineering, Washington University in St. Louis, St. Louis, Missouri 63130; Tel: (314) 935-6152; Fax: (314) 935-7448; Email: lhwang@biomed.wustl.edu.

1083-3668/2008/13(4)/044009/5/$25.00 © 2008 SPIE

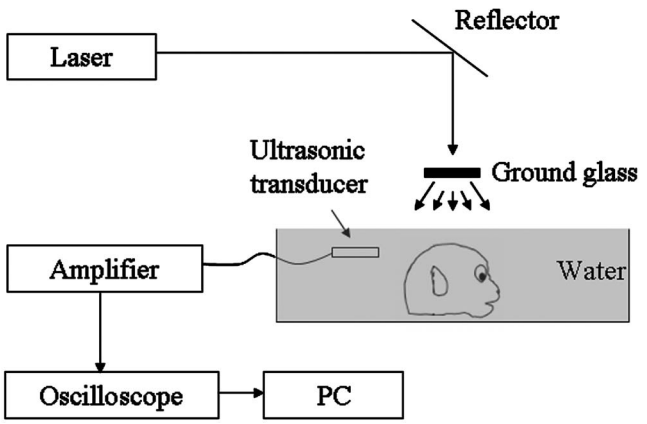

Fig. 1 Diagram of experimental setup.

immediately after the head was harvested. The first PAT experiment was performed on the fifth day after the animal was sacrificed. Before the experiment, the hairs on the head were shaved off to reduce the potential attenuation of optical and acoustic waves. The dimensions of the head in the axial view are about 9×7 cm, and the measured skull thickness is ~ 2 mm.

Before the experiment, the ultrasound transducer was aligned to point to the scanning center. The head sample was then held in a water tank and immersed in water. The location of the water tank was adjusted so that the sample was at the central scanning region. During the data acquisition, the ultrasound detector scanned the sample circularly for 240 steps, with a scanning radius of 10 cm. A backprojection algorithm[23] was employed to reconstruct an image. The laser wavelength used in all experiments was 1064 nm.

After the initial experiment, the skull was opened and the monkey brain was exposed. We found that the brain tissue still looked fresh when the skull was opened, because it is hard for formalin to penetrate the skull. We also found that fluid blood still remained in the major blood vessels, which provided optical contrast.

Before imaging the exposed brain, the skull bone was put back on the monkey brain to keep the brain in its original shape. Then the head sample was immersed in the 10% formalin solution. After the brain was fixed by formalin, the skull bone could be removed without altering the shape of the brain. The formalin solution also helped to solidify the blood in the blood vessels so that blood would not diffuse into water when the brain was immersed.

Next, we imaged the exposed brain with the skull on but with the scalp and dura mater removed. The relative location between the skull and blood vessels might have changed slightly and may have had an effect on the incident angle of the PA signals. After this process, the skull was removed and the exposed brain was imaged again.

To understand the effect of the skull bone on PA signals, we characterized the acoustic properties of the skull bone using PA signals. A 50-μm-diameter, 1-cm-long human hair was used as the PA target, and the hair was oriented parallel to a transducer surface in the detection plane. At the beginning of the measurement, the transducer was used to detect the PA signal from the hair directly. Then the skull bone was placed between the transducer and the hair, and PA signals were detected again. Since the skull bone is not flat, its curvature may introduce uncertainties in the incident angles at which the PA pulses strike the skull. To minimize this effect, we oriented the central part of the skull, which is relatively flat, to be parallel to the transducer surface and in the direct path of wave propagation from the PA source to the transducer. During the experiment, the skull was rotated to different angles to provide different incident angles to the PA pulses. The two ultrasound transducers used in detecting PA signals had center frequencies at 1 MHz (V303, Panametrics, Waltham, MA) and 2.25 MHz (V323, Panametrics, Waltham, MA), respectively. The monkey skull thickness in the central part was also measured with a caliper and found to vary from 1.45 mm to 2.46 mm, with an average value of 1.95 mm.

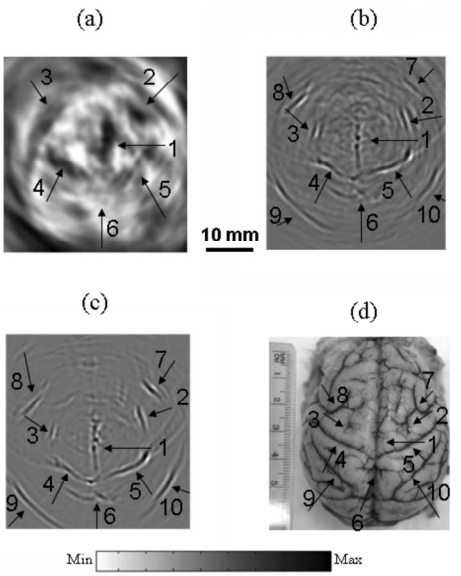

Fig. 2 (a) PAT image of a rhesus monkey brain with intact scalp and skull bone; (b) PAT image of the monkey brain with the skull bone only; (c) PAT image of the exposed monkey brain; (d) photograph of the exposed monkey brain. The blood vessels that can be identified from the PAT image have matching numbers.

In all the above PAT experiments, we estimated that the fluence delivered by each laser pulse was ~ 50 mJ/cm^2 at 1064 nm, which complies with the ANSI safety standard.[24]

3 Results

The reconstructed PAT images and a photograph of the exposed brain cortex for the rhesus monkey are shown in Fig. 2. Fig. 2(a) shows a PAT image of the monkey brain cortex with the intact scalp and skull. Fig. 2(b) shows an image with the skull only, and Fig. 2(c) shows an image of the exposed brain. Fig. 2(d) is a photograph of the exposed monkey brain. Note that the shape of the brain in Fig. 2(d) had changed slightly since there was no support by the skull bone, and the dura mater had also been removed to expose the brain.

In Fig. 2(a), through the intact scalp and skull, six vascular structures can be identified from the PAT image. With the skull only, Fig. 2(b) shows many more details of the monkey brain cortex than Fig. 2(a). Fig. 2(c) shows the brain cortex with even greater clarity than Fig. 2(b), due to the lack of the

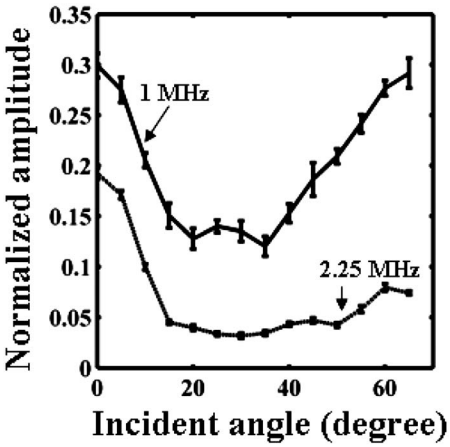

Fig. 3 PA signal amplitude of a human hair detected by a 1-MHz transducer (thick solid line) and a 2.25-MHz transducer (thin dashed line) after the signal propagates through a skull bone at different incident angles. All of the amplitudes were normalized by the signal amplitude detected when the skull was absent. The error bars shown on the curve are the standard deviations of 10 measurements.

skull effect. Note that since the monkey brain has a curved surface, but our PAT scan in this implementation is two-dimensional, Figs. 2(a)–2(c) look quite different than Fig. 2(d). However, we can still associate the corresponding blood vessels between them. We labeled the blood vessels using the same numbers in Figs. 2(a)–2(d). The field of view in the PAT image is also smaller than that of the photograph because of the limited laser beam size. Compared with Fig. 2(c), Fig. 2(a) shows similar main vascular structures, which have been labeled with the numbers 1–6 on the monkey brain cortex, except that structures 7–10 are not clearly visible in Fig. 2(a). However, the blood vessels shown in Fig. 2(a) are thicker than those in Fig. 2(c), which is probably due to optical attenuation in the scalp and dura mater. Again, compared with Fig. 2(c), Fig. 2(b) shows the brain cortex with a slightly reduced contrast due to the skull bone. To further quantify the similarity between Figs. 2(b) and 2(c), we calculated the two-dimensional correlation of these two images. The calculated correlation coefficient is 0.7. This result indicates that Fig. 2(b) exhibits most of the structures that have been shown in Fig. 2(c), even though the brain was covered by the skull bone. Therefore, the effect of the skull bone on PAT is not significant. In fact, the degradation of the image quality due to the scalp is stronger. Quantitative correlation between Figs. 2(c) and 2(a) is not applicable since the shape of the brain changed after the skull removal.

Fig. 3 shows the attenuation effect of the skull on PA signals. The normalized amplitude of the detected PA signals is shown as a function of the incident angle. For both 1-MHz and 2.25-MHz transducers, as the incident angle increases, the received signal amplitude decreases. Beyond ~35°, the received signal amplitude increases again. This effect may be explained by the generation of shear waves,[25] which we will discuss in detail next. Of the two transducers, the 1-MHz transducer received stronger signals.

At a normal incident angle for 1 MHz, the total PA signal loss due to the presence of the skull bone is 50 dB/cm. In the above calculations, we used an average sound speed of 2900 m/s and a density of 1900 kg/m^3 for the skull bone, a sound speed of 1500 m/s, a density of 998 kg/m^3 for water, and a skull thickness of 1.95 mm. If we remove the loss due to reflection, the insertion loss is 33 dB/cm, a value about 3 times that of a human skull.[26] Therefore, the ~2-mm-thick monkey skull has as much insertion loss as a ~6-mm-thick human skull. Since the thickness of a human skull ranges from 4 mm to 9 mm,[27] PAT may be able to image the human brain cortex as long as enough laser energy can penetrate the human scalp and skull.

4 Discussion

We showed that PAT can be applied through a relatively thick skull bone and that promising images can be obtained. In fact, due to their attenuations to both ultrasound and light, the scalp and the dura mater seem to have a larger effect than the skull on the image quality. We also expect that once the skull gets thicker, the distortion by the skull may become more severe, necessitating corrections for the distortion.

Besides the skull bone, the scalp and dura mater contribute to the degradation in image quality in Figs. 2(c) and 2(a). We do not expect the scalp and dura mater to have significant effects on ultrasound signals, but the presence of the scalp and dura mater might severely reduce the laser penetration, and then reduce the image's SNR. As a result, the effective photoacoustic bandwidth with sufficient SNR is reduced, leading to poorer spatial resolution. Fourier transformation of the experimental data indicates that the effective photoacoustic bandwidths at SNR=2 are 0.34 MHz, 0.70 MHz, and 0.77 MHz for Figs. 2(a)–2(c), respectively. In addition, the scalp and dura mater also generate PA signals, which can clutter the brain cortex images.

The propagation of ultrasound signals through the monkey skull needs further comment. Since the sound speed in the skull bone is approximately twice as fast as that in soft tissue,[26] the longitudinal wave has a critical incident angle of ~30° when sound propagates from soft tissue to the skull. In other words, once the incident angle is larger than 30°, the longitudinal wave will be totally reflected on the skull surface. In our PAT detection system, we detect PA signals on the horizontal plane of the monkey brain. At this detection location, signals from the blood vessels on the brain cortex are likely to have incident angles larger than 30° when they propagate toward the skull. Therefore, these signals would be totally reflected at the inner surface of the skull. However, we can still receive ultrasound signals generated from the blood vessels on the brain cortex. The signals we detected are probably from longitudinal–shear–longitudinal wave conversion. It is well known that at a boundary, the refracted waves consist of both longitudinal waves and shear waves. If the incident angle is beyond the critical angle for longitudinal waves, shear waves can still propagate beyond the boundary while longitudinal waves cannot. If the boundary is part of a layered material, the shear waves will convert back to longitudinal waves at the other boundary. Through this mechanism, we can still receive signals from blood vessels beyond the critical angle.

By the longitudinal–shear–longitudinal wave conversion, the wave propagation through a skull can avoid severe wavefront distortions caused by inhomogeneous sound speed,[25]

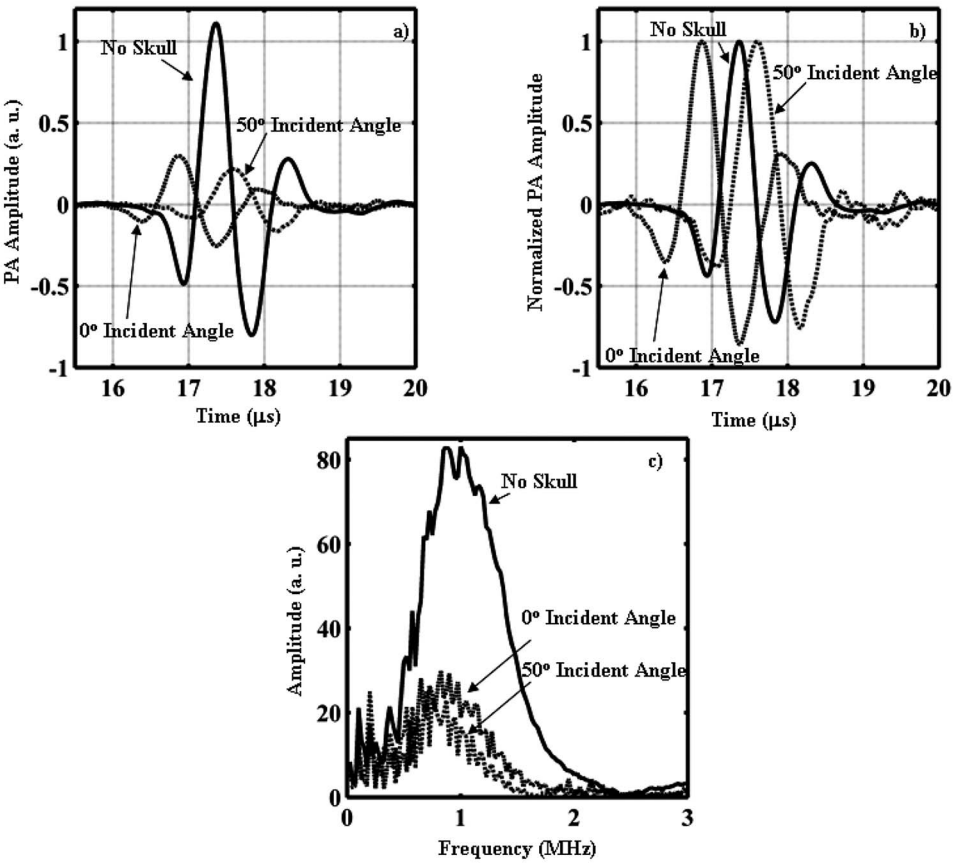

Fig. 4 PA waveforms from a human hair detected by a 1-MHz transducer. (a) Original PA waveforms; (b) PA waveforms normalized by their own peak amplitudes; (c) Fourier transforms of three waveforms in (a).

which usually occurs when ultrasound signals pass through a skull bone. The longitudinal wave speed in soft tissue is ~1500 m/s, and the shear wave speed in skull is ~1450 m/s. The similar propagation speeds of these two waves help to keep the wavefront from distorting severely when ultrasound signals pass through the skull.

To further understand the effect of longitudinal–shear–longitudinal wave conversion, we present the PA waveforms generated by the human hair in Fig. 4. Fig. 4(a) shows the PA signals received by the 1-MHz transducer after the signals passed through the skull bone with incident angles of 0° and 50°. The received PA signal when the skull bone is absent is also presented. The "No Skull" case shows the strongest amplitude due to the lack of skull attenuation, whereas the other two are attenuated by the skull. Fig. 4(b) shows the same PA waveforms, but the signals are normalized by their own peak values to show the first arrival times more clearly. We estimated the arrival time of each pulse at the rising edge (falling edge in this case) when the amplitude reaches 10% of the peak amplitude, which is more than twice the noise level. The arrival time is 16.1 μs for the "0° Incident Angle" case, 16.7 μs for the "No Skull" case, and 16.8 μs for the "50° Incident Angle" case. The measurement results of arrival times agree well with our earlier prediction. At the 50° incident angle, the photoacoustic signal passed through the skull by converting the longitudinal wave into a shear wave and then back into a longitudinal wave. Since the shear wave speed is similar to the sound speed in water, the "50° Incident Angle" case has a similar arrival time as the "No Skull" case. The "0° Incident Angle" case has a time lead because the signal passed through the skull as longitudinal waves, whereas the longitudinal wave speed in the skull is almost twice that in water.

Fig. 4(c) shows the Fourier transforms of the signals shown in Fig. 4(a). Whereas the center frequency for the "No Skull" case maintains 1 MHz, the center frequencies shift toward the lower frequencies for the "50° Incident Angle" and "0° Incident Angle" cases. The "50° Incident Angle" case shifts more than the "0° Incident Angle" case. This shift to lower frequencies is due to the strong attenuation of high-frequency components by the skull.

5 Conclusion

We have shown that PAT can overcome the effect of a relatively thick skull bone and that PAT brain cortex imaging of a relatively large animal is feasible. With the help of contrast agents, PAT can potentially image through even thicker skull bones. This result suggests that PAT may have the potential for human brain cortex imaging in infants or even adults.

Acknowledgments

This project was sponsored in part by National Institutes of Health Grant nos. R01 NS46214 and R01 EB000712.

References

1. S. L. Schreiber, E. Stolz, and J. M. Valdueza, "Transcranial ultrasonography of cerebral veins and sinuses," *Eur. J. Ultrasound* **16**, 59–72 (2002).
2. G. Ancora, M. Lanari, T. Lazzarotto, V. Venturi, E. Tridapalli, F. Sandri, M. Menarini, E. Ferretti, and G. Faldella, "Cranial ultrasound scanning and prediction of outcome in newborns with congenital cytomegalovirus infection," *J. Pediatr. (St. Louis)* **150**(2), 157–162 (2007).
3. F. Fry, N. Sanghvi, R. Morris, J. Clendenon, K. Dines, J. Patrick, and S. Goss, "Ultrasonic diagnostic system for interactive interrogation of adult brain through intact skull," *Invest. Radiol.* **17**, 463–469 (1982).
4. K. Dines, F. Fry, J. Patrick, and R. Gilmor, "Computerized ultrasound tomography of the human head: Experimental results," *Ultrason. Imaging* **3**, 342–351 (1981).
5. J. Ylitalo, J. Koivukangas, and J. Oksman, "Ultrasonic reflection mode computed tomography through a skullbone," *IEEE Trans. Biomed. Eng.* **37**, 1059–1066 (1990).
6. D. N. White, J. M. Clark, J. N. Chesebrough, M. N. White, and J. K. Campbell, "Effect of skull in degrading the display of echoencephalographic B and C scans," *J. Acoust. Soc. Am.* **44**, 1339–1345 (1968).
7. S. Daverson, D. H. Evans, and D. C. Bouch, "The effects of temporal bone on transcranial Doppler ultrasound beam shape," *Ultrasound Med. Biol.* **26**(2), 239–444 (2000).
8. S. W. Smith, D. J. Phillips, O. T. von Ramm, and F. L. Thurstone, "Some advances in acoustic imaging through the skull," in *Ultrasonic Tissue Characterization II*, M. Linzer, Ed., NBS Pub. #525, pp. 209–218 (1979).
9. S. W. Smith, K. Chu, S. F. Idriss, N. M. Ivancevich, E. D. Light, and P. D. Wolf, "Feasibility study: Real-time 3-D ultrasound imaging of the brain," *Ultrasound Med. Biol.* **30**(10), 1365–1371 (2004).
10. N. M. Ivancevich, J. J. Dahl, G. E. Trahey, and S. W. Smith, "Phase-aberration correction with a 3-D ultrasound scanner: Feasibility study," *IEEE Trans. Ultrason. Ferroelectr. Freq. Control* **53**(8), 1432–1439 (2006).
11. M. Tanter, J. L. Thomas, and M. Fink, "Focusing and steering through absorbing and aberrating layers: Application to ultrasonic propagation through the skull," *J. Acoust. Soc. Am.* **103**, 2403–2410 (1998).
12. R. Seip, P. VanBaren, and E. Ebbini, "Dynamic focusing in ultrasound hyperthermia using implantable hydrophone arrays," *IEEE Trans. Ultrason. Ferroelectr. Freq. Control* **41**(5), 706–713 (1994).
13. J. F. Aubry, M. Tanter, J. Gerber, J. L. Thomas, and M. Fink, "Optimal focusing by spatio-temporal inverse filter. II. Application to focusing through absorbing and reverberating media," *J. Acoust. Soc. Am.* **110**(1), 48–58 (2001).
14. C. G. A. Hoelen, F. F. M. de Mul, R. Pongers, and A. Dekker, "Three dimensional photoacoustic imaging of blood vessels in tissue," *Opt. Lett.* **23**, 648–650 (1998).
15. R. A. Kruger, D. R. Reinecke, and G. A. Kruger, "Thermoacoustic computed tomography—technical considerations," *Med. Phys.* **26**, 1832–1837 (1999).
16. R. O. Esenaliev, A. A. Karabutov, and A. A. Oraevsky, "Sensitivity of laser opto-acoustic imaging in detection of small deeply embedded tumors," *IEEE J. Sel. Top. Quantum Electron.* **5**, 981–988 (1999).
17. K. P. Köstli, D. Frauchiger, J. J. Niederhauser, G. Paltauf, H. P. Weber, and M. Frenz, "Optoacoustic imaging using a three-dimensional reconstruction algorithm," *IEEE J. Sel. Top. Quantum Electron.* **7**, 918–923 (2001).
18. M. Xu and L.-H. Wang, "Biomedical photoacoustics," *Rev. Sci. Instrum.* **77**(4), 041101 (Apr. 2006).
19. X. Wang, Y. Pang, G. Ku, X. Xie, G. Stoica, and L. V. Wang, "Noninvasive laser-induced photoacoustic tomography for structural and functional imaging of the brain *in vivo*," *Nat. Biotechnol.* **21**, 803–806 (2003).
20. M. Li, J. Oh, X. Xie, G. Ku, W. Wang, C. Li, G. Lungu, G. Stoica, and L. V. Wang, "Simultaneous molecular and hypoxia imaging of brain tumors *in vivo* using spectroscopic photoacoustic tomography," *Proc. IEEE* **96**(3), 481–489 (2008).
21. Y. Xu and L. V. Wang, "Rhesus monkey brain imaging through intact skull with thermoacoustic tomography," *IEEE Trans. Ultrason. Ferroelectr. Freq. Control* **53**(3), 542–548 (2006).
22. F. J. Fry, "Transskull transmission of an intense focused ultrasonic beam," *Ultrasound Med. Biol.* **3**,(2–3), 179–184 (1977).
23. M. H. Xu, Y. Xu, and L. H. V. Wang, "Time-domain reconstruction algorithms and numerical simulations for thermoacoustic tomography in various geometries," *IEEE Trans. Biomed. Eng.* **50**, 1086–1099 (2003).
24. Laser Institute of America, American National Standard for Safe Use of Lasers ANSI Z136.1-2000, American National Standards Institute Inc., New York (2000).
25. G. T. Clement, P. J. White, and K. Hynynen, "Enhanced ultrasound transmission through the human skull using shear mode conversion," *J. Acoust. Soc. Am.* **115**, 1356–1364 (2004).
26. F. Fry and J. Barger, "Acoustical properties of the human skull," *J. Acoust. Soc. Am.* **63**, 1576–1590 (1978).
27. A. Adeloye, K. R. Kattan, and F. N. Silverman, "Thickness of the normal skull in the American blacks and whites," *Am. J. Phys. Anthropol.* **43**, 23–30 (1975).